The effects of mean atmospheric forcings of the stable atmospheric boundary layer on wind turbine wake

Kiran Bhaganagar and Mithu Debnath

Articles you may be interested in

Effects of a three-dimensional hill on the wake characteristics of a model wind turbine
Phys. Fluids **27**, 025103 (2015); 10.1063/1.4907685

Effects of incoming surface wind conditions on the wake characteristics and dynamic wind loads acting on a wind turbine model
Phys. Fluids **26**, 125108 (2014); 10.1063/1.4904375

Large eddy simulation study of scalar transport in fully developed wind-turbine array boundary layers
Phys. Fluids **23**, 126603 (2011); 10.1063/1.3663376

Large-eddy simulation of a very large wind farm in a stable atmospheric boundary layer
Phys. Fluids **23**, 065101 (2011); 10.1063/1.3589857

Large eddy simulation study of fully developed wind-turbine array boundary layers
Phys. Fluids **22**, 015110 (2010); 10.1063/1.3291077

The effects of mean atmospheric forcings of the stable atmospheric boundary layer on wind turbine wake

Kiran Bhaganagar[a)] and Mithu Debnath
Department of Mechanical Engineering, University of Texas at San Antonio, San Antonio, Texas 78249, USA

Interactions between the nocturnal atmospheric boundary layer (ABL) and wind turbines (WTs) can be complicated due to the presence of low level jets (LLJ), a region which creates wind speeds higher than geostrophic wind speed. A study has been performed to isolate the effect of mean forcings of the ABL on turbulence energetics and structures in the wake of WT. Large eddy simulation with an actuator line model has been used as a tool to simulate a full-scale 5-MW WT under two different realistic atmospheric states of the stable ABL corresponding to low- and high-stratification. The study clearly demonstrates that the large-scale forcings of thermally stratified atmospheric boundary characterized by shear- and buoyancy-driven turbulence significantly influence the wake structure of a wind turbine. For the WT in low-stratified ABL, the jets occur above the WT resulting in a strong mixed layer behind the WT. High turbulence results in a faster wake recovery. For the WT in high-stratified ABL, the jets occur near the hub-height resulting in an asymmetric wake structure. The jets confine the mixing to hub-height resulting in a slower wake recovery. Vertical shear causes the interaction of the root- and lower-tip vortices resulting in the instability of the root vortex leading to an enhanced shear stress and turbulent kinetic energy. The tip vortices exhibit mutual inductance between adjacent vortex filaments resulting in vortex merging. LLJs are an important metric associated with mean atmospheric forcings that dictate the turbulence generated in WT wake and the wake recovery of a WT in a stable ABL. © *2015 AIP Publishing LLC*. [http://dx.doi.org/10.1063/1.4907687]

I. INTRODUCTION

Full-scale horizontal axis wind turbines (WTs) operate in atmospheric boundary layer (ABL) with atmospheric forcings playing an important role on the wake generated behind the WT. ABL and WT interactions result in strong wake turbulence that adversely impacts the overall performance of WT (Wharton and Lundquist, 2012). Recent efforts in WT research toward improved prediction of wake effects clearly indicate the role of realistic atmospheric inflow conditions (Hu *et al.*, 2012 and Mirocha *et al.*, 2014). In particular, the structure of the ABL under stable stratification is extremely complicated as the mean state of a stable ABL has a region of higher wind speeds than the geostrophic wind speed referred to as low level jets (LLJ). Hence, understanding the interactions between the ABL and WTs in stable stratification conditions is important.

In the Cooperative Atmosphere-Surface Exchange Study-99 (Cases-99) field experiments, wind profiles have confirmed that LLJ persist through the night with their height varying between 90 m and 300 m above the surface depending on stratification during the night (Poulos *et al.*, 2002). Other studies have also confirmed that LLJ shift downward with increasing stratification (Banta, 2008). Hence, for a typical full WT with a hub height (*H*) of 90 m, the LLJ location can occur anywhere from the hub height to above the WT during the night. As LLJ

[a)]Author to whom correspondence should be addressed. Electronic mail: kiran.bhaganagar@utsa.edu

7, 013124-1

are regions of higher wind speed, the location and the strength of LLJ will alter the wind shear, while lowered LLJ will result in larger mean velocity gradients than LLJ at higher heights. Thus, for the same geostrophic conditions, the resultant wind shear changes with stratification due to LLJ. Wind shear generates turbulence through shear production of turbulent kinetic energy (TKE). As wind shear changes with stratification, an increased stratification alters the shear-generated turbulence. It is known that increased stratification also damps the turbulence. The competing roles of increased shear vs. increased damping in higher stratification now dictate the resultant turbulence in the turbine wake region. While wind shear has been recognized as an important parameter that influences WT wake (Vermeer *et al*., 2003), the implications of interaction between LLJ and WTs have not been explored in depth. This is the focus of our paper. In our study, we isolate the effects of large-scale mean forcings (i.e., mean wind velocity and temperature and surface mean heat and momentum flux) on WT wake so that we can concentrate on the competing roles of increased TKE production due to wind shear vs. increased damping due to thermal stratification. Turbulence in the wake region is a balance of turbulence generation, damping, and transport by mean and fluctuations. By studying the energetics—the balance of TKE transport equation—the turbulence state will be understood. The turbulence structures will provide the large-scale features of the wake region. Both the energetics and the turbulence structures together will define turbulence in the turbine wake region. This study is an important step toward demonstrating the need for including realistic turbine/atmosphere interactions.

The turbulence structure of WT wake is a consequence of the nonlinear interactions between atmospheric inflow conditions, WT generated turbulence, and atmospheric stratification effects. The dominant structure in the near-wake of WTs is a vortex system comprising tip- and root-vortices (Okulov and Sørensen, 2007). The particle image velocimetry (PIV) measurements by Whale *et al*. (1996) and Massouh and Dobrev (2007) and the hot-wire anemometer measurements by Chamorro and Porte-Agel (2009) and Zhang *et al*. (2012) have demonstrated helical tip vortices due to the vorticity shed from the blade tips. Hu *et al*. (2012) and Yang *et al*. (2012) using a high resolution PIV system demonstrated helical trajectory of the tip vortex for WTs subjected to ABL inflow conditions. The instability of the helical filament will dictate the resultant turbulent structures in the turbine wake.

Widnall (1972) hypothesized for a helical vortex filament the existence of at least three modes of inviscid instability: short-wave instability which exists on all curved filaments, a long-wave mode, and a mutual inductance mode which appears as the pitch of the helix decreases and the neighboring filament interacts strongly. Numerical and experimental studies have noticed the existence of the mutual inductance mode of instability in the rotor wake region. Felli *et al*. (2011) experimentally revealed the instability modes hypothesized by Widnall (1972). Recently, Sherry *et al*. (2013) captured the tip vortex mutual inductance leading to the merging of the vortices. Numerical simulations of Sørensen and Shen (2002) and Ivanell *et al*. (2010) and the experimental observations of Felli *et al*. (2011) have confirmed that the mutual inductance mode is associated with vortex pairing. However, those studies have been limited to uniform inlet flow conditions without realistic atmospheric forcing conditions.

Many studies have focused on idealistic inflow conditions and have not included the role of large-scale forcings of the atmosphere on turbulence structures. The motivation of our study is to understand the role of the realistic mean structure of the atmosphere on the energetics and the vortex system in the near-wake region of WTs. The primary questions that we will address are:

(1) How does the strength and height of LLJ affect wake turbulence? How does the turbulence generated in LLJ affect wake turbulence?
(2) What are the differences in the energetics and tip/root vortex interactions due to increasing stability? What are the consequences with respect to wake recovery and wake strength?

The study is motivated by the fact that wind patterns upstream of the wind turbines are governed by the atmospheric boundary layer flow that develops over the surface under the combined influence of atmospheric stratification, surface temperature, surface cooling rate,

geostrophic wind conditions, topographical location, and Coriolis force. Further, the surrounding ABL wind interacts with the turbulence generated by the wind turbine. Hence, for an accurate estimation of wake effects of the wind turbine, it is imperative to conduct the study using exact wind patterns at that location. For this purpose, though computationally expensive, site-specific, precursor ABL simulations are initially conducted to obtain these wind patterns (temperature, velocity, and pressure fields). The large-scale forcings of the wind conditions introduced into the domain are representative of the realistic ABL forcings, which is the uniqueness of the proposed study. In particular, the exact wind conditions at two different instances of the diurnal cycle are simulated. These two instances correspond to two different stability regimes of the atmosphere. This study is a significant paradigm shift from existing studies based on imposing idealized wind conditions towards replicating an instance of the diurnal cycle. It is to be noted that even if the blade rotation is kept fixed, atmospheric loadings acting on the turbine will be different due to the inherent differences in the wind patterns (such as wind shear, temperature gradients) at different instances of the diurnal cycle. It also suggests the tip speed ratio may or may not be similar for different instances, and the wake cannot be characterized based on tip speed ratio metric.

Large eddy simulation (LES) has been demonstrated to be a valid numerical tool to simulate weakly/moderately stable ABL in a continuous state of turbulence. Ohya *et al*. (1997) used LES to demonstrate that turbulence is suppressed with increasing stability in a stable ABL. Zhou and Chow (2012) demonstrated using LES that stronger surface cooling results in a larger shear exponent (the measure of the shear of mean wind). Huang and Bou-Zeid (2013) performed LES and observed that increasing stability results in lowered LLJ, a mean temperature profile with stronger temperature gradient, and an increase in turbulence production around the location of LLJ. Lu and Porte-Agel (2011) performed LES for an idealized wind farm in a weakly stratified ABL and demonstrated the presence of high vertical and horizontal wind shear. Their study was limited by the atmospheric stability conditions when LLJ occur above the WT. Moreover, high turbulence was introduced at the inlet of the WT resulting in strong wake turbulence and vortex breakup close to the turbine.

In our study, we used LES as a tool to simulate WTs in a stable ABL. The mean state of the stable atmosphere for the WT simulations was obtained from precursor ABL simulations. Our analysis was conducted using two different atmospheric stability conditions such that the ABL is in a continuous turbulent state without intermittency. We selected the atmospheric stability to represent nighttime conditions based on the observational evidence from Cases-99 experiments. In this study, we simulated the case described in Kosovic and Curry (2000) that imposed a steady surface-cooling rate of -0.25 K/h. We also simulated a case with a higher cooling rate. The conditions selected by Kosovic and Curry (2000) matched the Beaufort Sea Arctic Stratus Experiment (BASE) to resemble a clear-air stable ABL driven by a moderate surface-cooling rate. We selected a surface cooling rate of -1.0 K/h for the higher atmospheric stability case based on simulations by Zhou and Chow (2012) who used a surface cooling rate of -0.25 K/h, -0.75 K/h, and -1.25 K/h, whereby the turbulence is in a continuous state. The two stability conditions correspond to the following conditions: (1) low stratification (LS)—LLJ occur at a height of 180–200 m and a surface temperature of $263\,°$K and (2) high stratification (HS)—LLJ occur at a height of 80–100 m with a surface temperature of $256°$K.

This study is fundamental in nature and will improve our understanding of the wake turbulence of WTs in a stable ABL. To date, there has been very limited understanding on the effects of realistic atmospheric mean conditions on WT wakes. Ours is the first study to reveal the dynamics of turbulence in the wake of wind turbines subjected to realistic mean atmospheric forcings.

This paper is organized as follows: In Sec. II, the details of a large eddy simulation numerical model are described. The tool has been validated for a stable ABL with existing measurements as well as inter-model comparison. The validation results for the stable ABL simulations are presented in Sec. III. The results of ABL simulations are presented in Sec. IV. The results of two stratification cases, which we refer to as LS and HS cases, are presented in Sec. V. Conclusions are presented in Sec. VI.

II. NUMERICAL METHODOLOGY

In this study, we performed numerical simulations using LES methodology. We used the Open Foam-based simulator for offshore wind farm applications (SOWFA) tool for solving the filtered, 3D incompressible Navier-Stokes equations using the Boussinesq assumption to generate the buoyancy forces (Churchfield *et al.*, 2011). Churchfield *et al.* (2013) improved the SOWFA tool with the capability to handle Open Foam-based subgrid scale models. We modeled the subgrid scale stresses using the Smagorinsky model and used the surface cooling rate as a boundary condition (Basu *et al.*, 2008). Churchfield *et al.* (2013) demonstrated that the SOWFA solver standard Smagorinsky model produced similar mean velocity profiles of wind speed, potential temperature, and variance profiles to the standard Gewex Atmospheric Boundary Layer Study (GABLS) LES model inter-comparison results (Beare *et al.*, 2006).

We defined the instability of the stratified atmospheric boundary layer with an initial potential temperature flux. The cooling rate was specified at the surface, and the initial potential temperature profile was set to $265\,^{\circ}$K. We performed fine mesh refinements by refining the wake region with a grid size of $0.75\,$m. The time step used for the simulation was $0.5\,$s, and a random perturbation of $0.1\,$K was applied to the bottom $100\,$m of the domain at initialization to trigger turbulence. We carried out simulations for a total of $40\,000\,$s.

Following the work of Sorensen and Shen (2002), we approximated the rotor using the actuator line model (ALM). In the ALM, the body forces are distributed radially along lines, which represent the blades of the WT. The advantage of representing the blade by airfoil data is that fewer grid points are needed to capture the influence of the blades than would be needed for simulating the actual geometry of the blades. ALM takes into account blade motions and their mixing mechanisms, which is important for simulating realistic WT wakes.

In the LES solver, ALM has been implemented as follows: Let the tangential and axial velocities of the incident flow be denoted as V_θ and V_a, respectively. The local velocity relative to the rotating blades is given as $V_{rel} = (V_\theta - \Omega r, V_a)$, where r is the radius of the blade and Ω is the angle of rotation. The angle of attack is defined as $\alpha = \varphi - \varsigma$, where $\varphi = \tan^{-1}\left(\frac{V_a}{(\Omega r - V_\theta)}\right)$ is the angle between V_{rel} and the rotor plane and ζ is the pitching angle. The turbine-induced force per radial unit length is given as

$$f = 0.5\rho V_{rel}^2 c(C_L e_L + C_D e_D),\tag{1}$$

where $C_L = C_L(\alpha, \mathrm{Re})$ and $C_D = C_D(\alpha, \mathrm{Re})$ are the lift- and drag-coefficients, respectively. The chord length is c, and e_L and e_D are the unit vectors in the direction of the lift and the drag, respectively.

The rotor blades are discretized by a finite number of actuator points. The lift and drag forces computed at these actuator points (from Eq. (1)) are obtained by determining the local flow velocity and angle of attack that is then applied to an airfoil lookup table. The applied blade forces are distributed smoothly to avoid singular behavior and numerical instability. The blade forces are distributed along and away from the actuator lines in a three-dimensional Gaussian manner through the convolution of the computed local load f (Eq. (1)) and a regularization kernel as follows:

$$F = -\sum_n \sum_m f \exp\left[-\left(\frac{|r|}{\varepsilon}\right)^2\right]\frac{1}{\varepsilon^3 \pi^{3/2}},\tag{2}$$

where $|r|$ is the distance from the grid cell to the actuator point and ε is the Gaussian radius.

The computed blade loads are projected as volumetric body forces (F) in the momentum equations using a body force term as follows:

$$\frac{Du_i}{Dt} = -2\varepsilon_{ijk}\Omega_j u_k - \frac{\partial p}{\partial x_i} - \frac{\partial R^D_{ij}}{\partial x_j} + \left(\frac{\rho_b}{\rho_o} - 1\right)g + F,\tag{3}$$

where the first term on the right-hand-side is the Coriolis force, second term is the pressure gradient, third term is the subgrid momentum fluxes, the fourth term is the buoyancy term and the last term is the body force term. The effect of the body force term in Eq. (1) is a pressure jump across the actuator line and the formation of bound and trailing vorticity.

Lu and Porte-Agel (2011) have successfully implemented similar methodology for WT under ABL conditions. The root and tip vortices were captured well. Jha *et al.* (2014) demonstrated important ALM parameters are the Gaussian radius, the grid resolution, and the actuator spacing. To date, there has been no clear-cut recommendation for ideal ALM parameters. Common practice includes using a small Gaussian radius, a width that would spread the force over a region similar to the actual force. As suggested by Troldborg *et al.* (2007, 2010), we used a ratio of 2 for the Gaussian radius to grid size, and we selected 60 points along the actuator line such that the spacing between the actuator points is less than the grid spacing. Finally, based on the recommendation of Zahle and Sorensen (2007), we used a finer resolution of 0.75 m in the wake region up to 10 rotor diameters to accurately capture the near-wake vortex structures.

It should be noted that the coordinate axis employed is: streamwise velocity (u) along the x-axis, spanwise velocity (v) along the y-axis, and wall-normal velocity (w) along the z-axis.

III. VALIDATION OF STABLE ATMOSPHERIC BOUNDARY LAYER SIMULATIONS

We used a moderately stable test case to represent the situation studied by Kosovic and Curry (2000) with an imposed steady surface cooling rate to validate the solver, which has served as a standard test case to study efficacy of LES models, including inter-comparison of multiple LES models in the GABLS (Beare *et al.*, 2006) and the Basu and Porte-Agel's (2005) scale-dependent dynamical LES model. The prescribed initial potential temperature profiles are mixed layers with a potential temperature of $265\,^{\circ}$K up to 100 m with an overlying inversion layer of strength of $0.01\,\mathrm{km}^{-1}$. A surface cooling of $-0.25\,$K/h is prescribed for 9 h so that a quasi-equilibrium is achieved. The prescribed geostrophic wind is 8 m/s with a Coriolis parameter of 1.39×10^{-4}/s. Stress-free and no penetration boundary conditions were used at the top of the computational domain. We applied the Monin-Obhukov similarity theory at the lower boundary as a wall model with coefficients ($\beta_{\mathrm{m}} = 4.9$, $\beta_{\mathrm{h}} = 7.8$) consistent with Beare *et al.* (2006). A random potential temperature perturbation of amplitude $0.1\,^{\circ}$K was applied below the height of 50 m. The domain was size 400 m, 400 m, 400 m. We performed convergence tests with a grid size of 12.5 m, 6.25 m, and 3.125 m and 1 m, and with Smagorinsky model coefficient $C_s = 0.08$–0.16.

Fig. 1 shows the profile of the mean streamwise velocity ($\overline{U}$), shear stress ($\overline{u'w'}$), and mean temperature ($\overline{T}$) for three of our cases with grid size $\Delta = 6.25$ m and $C_s = 0.1$, $\Delta = 6.25$ m and $C_s = 0.13$, and $\Delta = 3.125$ m and $C_s = 0.1$, where C_s is the ratio of the mixing length to horizontal grid length. Also shown are the results from the Lagrangian dynamic model of Stoll and Porte-Agel (2008), the scale-dependent dynamic LES model of Basu and Porte-Agel (2005), the results from the inter-comparison study (Beare *et al.*, 2006) consisting of the Sullivan *et al.* (1994) (National Center for Atmospheric Research model (NCAR) model), Khairoutdinov and Randall (2003) (CSU model), Esau (2004) (Nansen Environment and Remote Sensing Center (NERSC)) and Cuxart *et al.* (2000) (UIB model)), Raasch and Etling (1991) (IMUK model), and Lewellen and Lewellen (1998) (WVU model). We validated a grid size of 3.125 m is sufficient for a stable ABL in a continuous turbulent state as a base model. Our observations are consistent with the suggestions from the GABLS inter-comparison LES study of the stable ABL. The results are close to an extremely fine 1 m-resolution simulation.

A nocturnal jet, as predicted by Nieuwstadt's (1984) theoretical model, was observed by Stoll and Porte-Agel (2008), Kosovi and Curry (2000), and the model inter-comparison analysis of Beare *et al.* (2006). The grid resolution of 3.125 m and $C_s = 0.1$ and 0.132 predicted a close match of both the location and strength of LLJ. When the grid resolution is reduced to 6.25 m, differences are observed close to the surface. When C_s is reduced further, the results are found to match close to the surface as well (results not shown). Subgrid dissipation is proportional to $(C_s\Delta)^2$ (Lilly, 1967). Higher values of C_s give higher values of subgrid dissipation. Fig. 1(b)
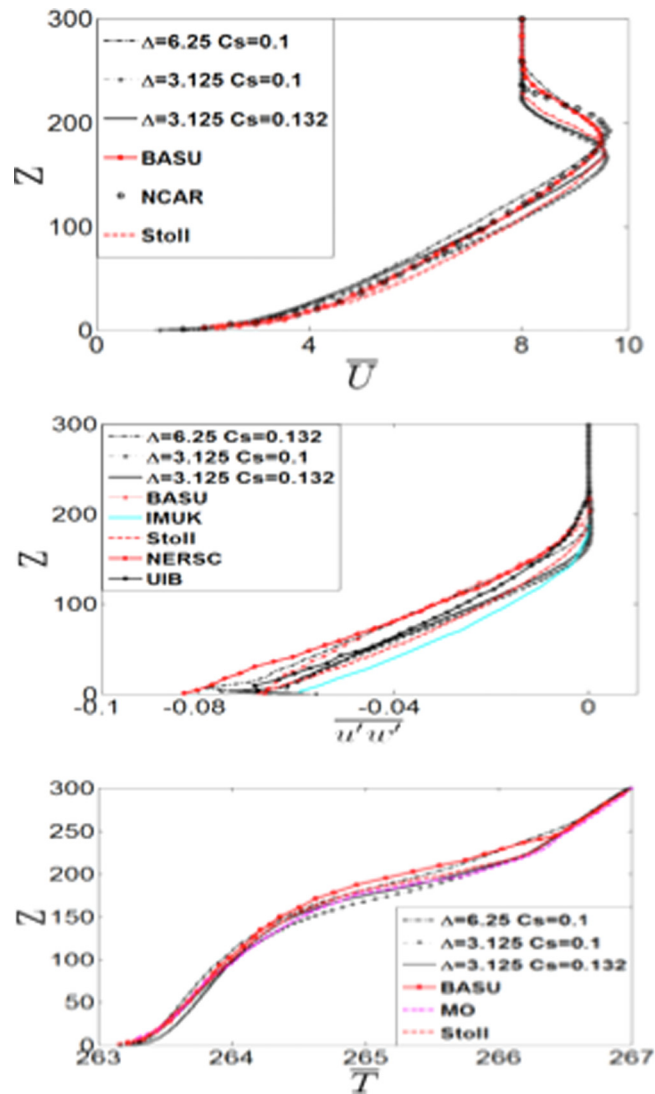
FIG. 1. Validation of (a) mean velocity, (b) streamwise turbulence intensity, and (c) mean temperature profile of a model with grid spacing $\Delta = 6.25$, Cs $= 0.1$, $\Delta = 3.125$, Cs $= 0.1$ $\Delta = 3.125$, Cs $= 0.132$ with Basu and Porte-Agel (2005) (BASU), Stoll and Porte-Agel (2008) (Stoll), Sullivan *et al.* (1994) NCAR, Esau (2004) NERSC model and Cuxart *et al.* (2000) Universitat de Les Illes Balears, Spain model (UIB), Raasch and Etling (1991) University of Hannover and Yonsei University model (IMUK), and Met Office UK model (MO).

shows the comparison of the profiles of shear stress. The model with 3.125 m grid resolution and Cs of 0.1–0.132 performs well. Similarly a grid resolution of 6.25 m and Cs $= 0.1$ performs well. We did not observe significant model sensitivity with the temperature profile as shown in Fig. 1(c).

Fig. 2 shows the time evolution of ABL parameters including surface heat flux and momentum flux for the case with a grid resolution of 3.125 m and Cs $= 0.132$. The momentum flux converges to an equilibrium solution much faster than the surface heat flux. The equilibrium values are compared with GABLS results (Bear *et al.*, 2006). Stoll and Porte-Agel (2008) obtained an ABL height in the range of 173 m to 182 m and Monin-Obhukov Length (L) in the range of 111 m to 113 m with grid resolution of 3.3 m to 9.9 m using the Lagrangian model. We obtained an ABL height of 181 m to 185 m with a grid size of 6.25 m, and a range of 162 m to 169 m with a grid size of 3.125 m. Both the trends as well as the range of ABL heights with increasing grid resolution match well with existing model results. Refining the mesh further to 1 m did not significantly change the ABL characteristics.
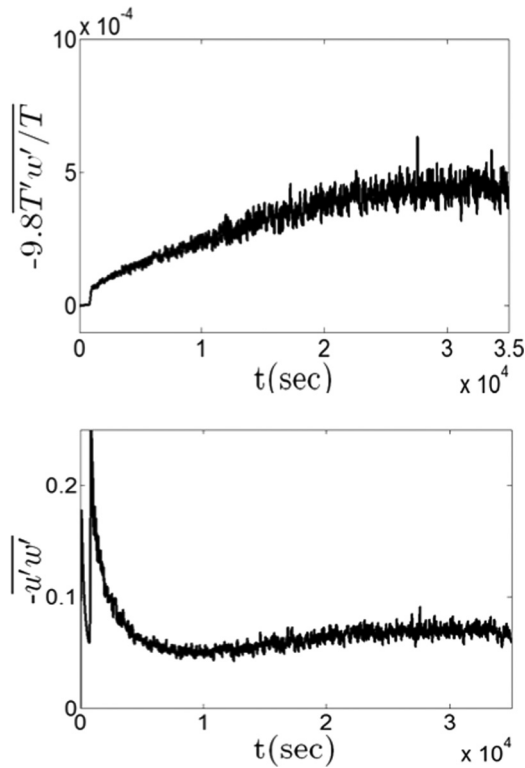
FIG. 2. Time evolution of (a) surface buoyancy flux and (b) momentum flux for a case with a grid resolution of 3.125 m and Cs = 0.132.

Next, we performed model sensitivity tests for the high stratification case. This involved validations with a grid resolution of 1–6.25 m and $C_s = 0.06$–0.15. Fig. 3(a) shows the mean velocity profile with a grid size of 6.25 m and $C_s = 0.09$–0.135. Higher C_s of 0.135 causes addition damping, hence deviation in the LLJ height and strength is observed. Similar behavior is observed in the mean temperature profile as seen in Fig. 3(b). Shear profile is shown in Fig. 3(c) and both $C_s = 0.09$ and $C_s = 0.1$ perform well. The results match well with the dynamic model LES of Huang and Bou-Zeid (2013), where they obtained LLJ at a height of 81–158 m for surface cooling rates corresponding to $-0.25\,\mathrm{K}\ \mathrm{h}^{-1}$ to $-2.5\,\mathrm{K}\ \mathrm{h}^{-1}$. With a surface cooling rate of $-1.0\,\mathrm{K}\ \mathrm{h}^{-1}$, the LLJ occurred at a height of 106 m, with a quasi-equilibrium surface temperature of 257 °K, and a quasi-equilibrium surface momentum flux of $-0.04\ \mathrm{m}^2\ \mathrm{s}^{-2}$. From our simulations, we obtained LLJ at a height of 102–114 m, surface temperature of 256 °K–257 °K, and surface momentum flux of 0.035–0.036 for different values of C_s with a grid size of 6.25 m. When we refined the mesh to 3.125 m, while significant differences in the ABL height were not observed, there was an improvement in surface momentum and buoyancy flux by 4% and 6%, respectively. Having confidence that the model generated accurate measurements for LLJ height, ABL height, surface momentum and buoyancy flux, surface temperature, and friction velocity for both the stratification cases to be considered, we continued our analysis. In Sec. IV, we present the results for ABL simulations with a grid resolution of 1 m in the wake region up to 10 rotor diameters. Outside the ABL, we used a grid resolution of 6.25 m.

IV. RESULTS: STABLE ATMOSPHERIC BOUNDARY LAYER UNDER LOW AND HIGH STRATIFICATION

We simulated ABL under LS and HS stratification conditions by prescribing the surface cooling rates of $-0.25\,\mathrm{K}\ \mathrm{h}^{-1}$ and $-1.0\,\mathrm{K}\ \mathrm{h}^{-1}$, respectively. The precursor ABL was simulated for 50 000 s. The statistics were computed when ABL reached a quasi-equilibrium state, which
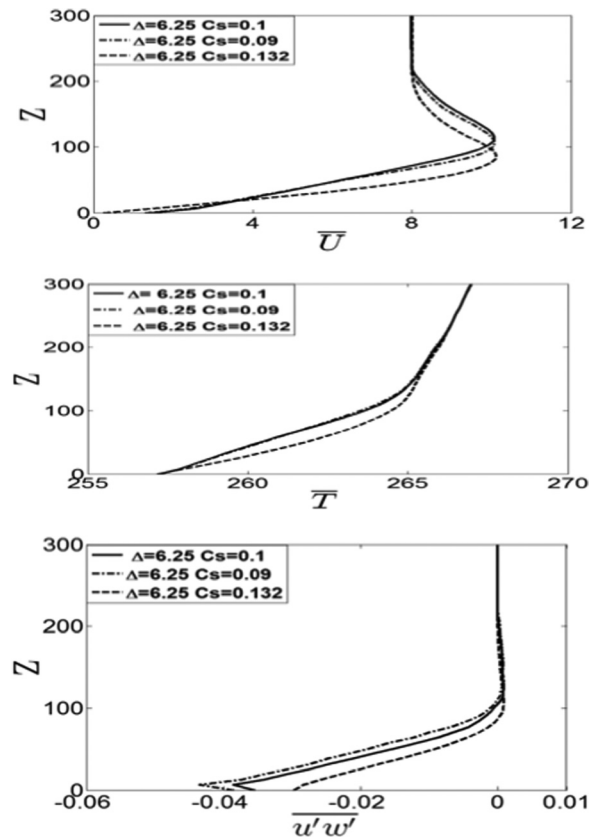
FIG. 3. Sensitivity to LES model parameter Cs with a grid size of 6.25 m for higher stratification case: (a) mean velocity profile, (b) mean temperature profile, and (c) $\overline{u'w'}$.

was defined as the state of ABL where the height of that layer and the surface fluxes of momentum and heat change relatively less with time, allowing turbulence to be close to equilibrium at any instant.

The horizontally and time-averaged velocity profiles of mean velocity and mean temperature for LS and HS cases are shown in Figs. 4(a) and 4(b), respectively. The structure of the mean atmospheric state under LS and HS was significantly different. For the former, the LLJ occurred at a height of $z = 185$ m with a strength of 9.5 m/s, for the latter, the LLJ occurred at a height of $z = 100$ m and with a strength of 10 m/s. The vertical velocity gradient for HS was steeper than LS, hence HS had a higher value of mean wind shear ($\frac{dU}{dz}$). It was consistent with observations that wind shear increases with increased stratification (Wharton and Lundquist, 2012).

The consequences of the differences in the mean structure of the atmosphere under LS and HS are quite significant with respect to a full WT with a diameter (D) of 126 m and hub height (H) of 90 m. The height of LLJ is one of the indicators for the ABL depth. It is interesting to note that as the ABL extends up to hub height for the HS, the upper-blade tip of the WT is outside the ABL, whereas as LLJ are at a height which is above the WT for LS, so the entire WT is within the ABL. Further, wind shear changes from a positive value below the LLJ to a negative value above them; hence, reversal of shear occurs between the hub height and the upper-blade tip of the WT for HS, whereas vertical shear reversal occurs above the WT for LS. Wind shear is fairly uniform above the LLJ due to a strong temperature inversion.

Figs. 5(a) and 5(b) show the horizontally averaged streamwise turbulence intensity and shear stress profile, respectively. Increasing stratification reduces the turbulence and therefore lowers turbulence intensities and shear stress for HS compared to LS, as expected.
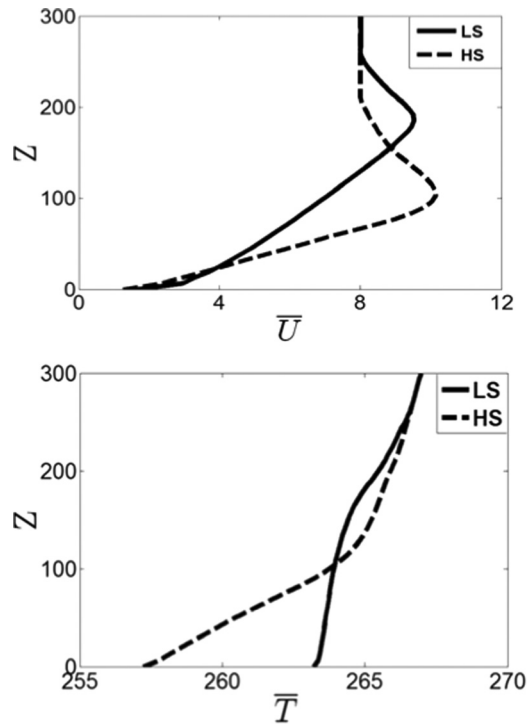
FIG. 4. Time-averaged profile of (a) mean velocity and (b) mean temperature of the stable ABL at LS and HS.
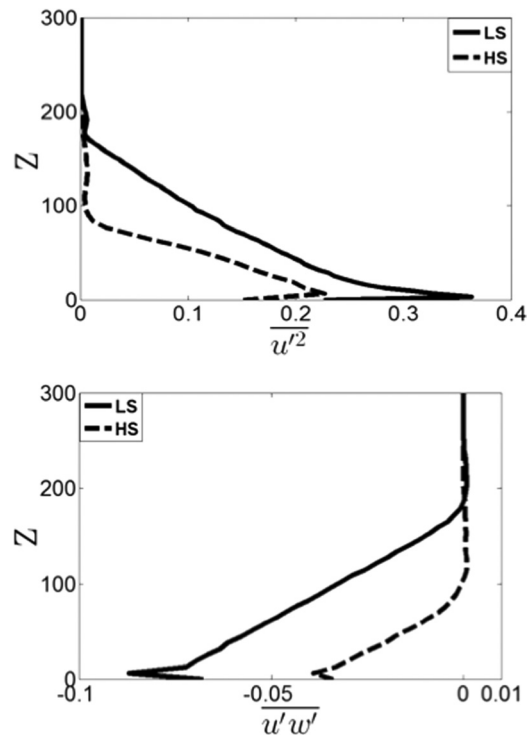

FIG. 5. Time-averaged profile of (a) turbulence intensity of streamwise velocity fluctuation and (b) $\overline{u'w'}$ of stable ABL as low and high stratification.

In Sec. V, we present the results for the wind turbine simulations subjected to mean ABL forcings. The rotation speed of the turbine has been fixed at 5 rpm. The corresponding tip-speed-ratio which is ratio of the tangential tip of the tip of the blade and the wind velocity is 4.9 for LS and 3.36 for HS, respectively.

V. RESULTS: WIND TURBINE SUBJECTED TO MEAN ABL FORCINGS

In this section, we discuss the effect of the mean ABL forcings subjected to two different stratifications (LS and HS) on the wake of WTs in a stable ABL. For this purpose, the precursor ABL simulations were performed to obtain a quasi-equilibrium mean state. We performed the WT simulations under the same boundary conditions and surface-cooling rate as the ABL. The simulations were performed with a grid size of 1-m resolutions up to 10-D downstream from the WT. A resolution of 3.125 m was used in regions away from the wake. The initial mean velocity and temperature profiles and the surface heat and momentum flux for the WT simulations were obtained from precursor ABL simulations. The turbulence state generated from the ABL simulation had peak amplitude close to the surface of 4% of inflow velocity. To the ABL mean state, we added artificial 3D periodic, homogenous, isotropic turbulence with 4% TKE as inflow conditions, and we performed the simulations for 180 s. The statistics were averaged in the last 80 s after the initial transience has passed.

We analyzed energetics (balance terms of the TKE transport equation) and turbulence structures in the WT wake, which together define the turbulence. TKE generated in the wake region is primarily a balance of the shear production and buoyancy damping. The shear production of TKE is the transfer of energy from large-scale to small-scale turbulence and is given as $-\overline{u'w'}\frac{dU}{dz}$. High velocity gradients and high Reynolds stresses lead to higher turbulence production. The production from buoyancy term $\overline{T'w'}\frac{dT}{dz}$ contributes to turbulence damping due to a negative temperature gradient. In Sec. V A, we present the flow statistics.

The dominant turbulence structures in the wake-region of the WTs are primarily blade tip and root vortex. Various vortex detection algorithms have evolved to identify vortices in turbulent flows. A pressure minimum is a generally used criterion to detect vortex centers. Having demonstrated that a pressure minimum might not be a sufficient criterion (as viscous effects might eliminate pressure minima), Jeong and Hussain (1995) developed the λ_2 criterion to extract the dominant vortical structure of the flow. This method defines a vortex as a region where the second largest eigenvalue of $S_{ij}S_{ij} + \Omega_{ij}\Omega_{ij}$ (S_{ij} and Ω_{ij} are the symmetric and anti-symmetric components of the velocity gradient tensor) is negative. In Sec. V B 2, we use the λ_2 criterion to extract the hub and the tip vortex.

A. Energetics

1. Mean velocity profile and velocity deficit

We present the contour plot of time-averaged streamwise velocity ($\overline{U}$) at the center plane, i.e., $y = 0$ for LS and HS in Figs. 6(a) and 6(b), respectively. WT has been placed at $x/D = 0$. Under ABL conditions (Sec. IV), the jets occur between $z/H = 1.8$–2.5 and $z/H = 1$–1.5 for LS and HS, respectively. The LLJ persist even with the presence of WT. Due to the jets at hub height for HS, the WT faces a higher velocity at hub height under HS than LS. As the jets are stronger and occur lower in height for HS; hence, the vertical variation of $\overline{U}$ is quite significant between the WT blade tips, i.e., $z/H = 0.3$ (lower-blade tip) and $z/H = 1.7$ (upper-blade tip). A stronger asymmetry in the mean structure between the lower- and upper-portion of the wake is present for HS.

In the near-wake region, energy is extracted from the incoming flow, thus producing a wake region with reduced mean velocity. To evaluate the deficits generated in the wake region, mean velocity deficit defined as $(\overline{U} - \overline{U_o})/\overline{U_o})$ has been plotted in Figs. 6(c) and 6(d) for LS and HS, respectively. Here, $\overline{U_o}$ is the time-average streamwise ABL velocity at the inlet.

The ABL under LS extends to above the WT height; hence, the entire WT is within the boundary layer. Strong velocity deficits are created at both the blade tips. Due to higher
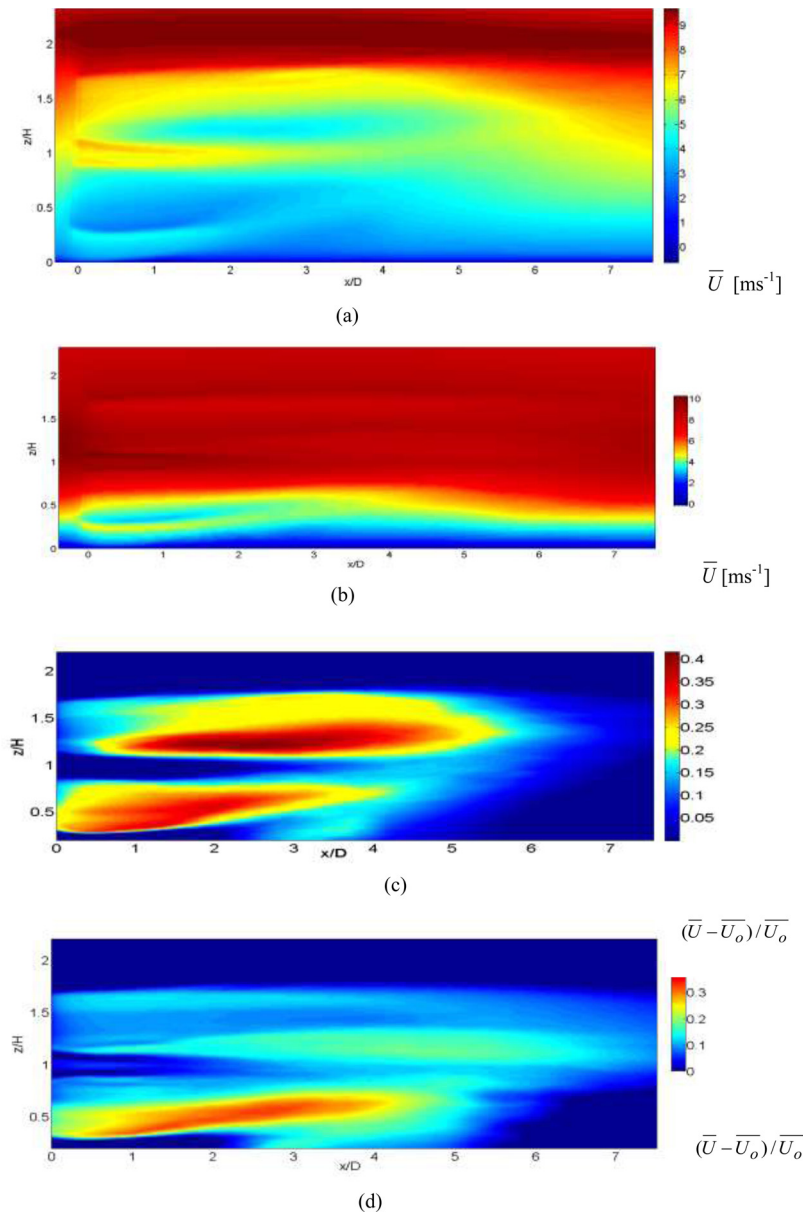
FIG. 6. (a) Time-averaged streamwise velocity for LS, (b) Time-averaged streamwise velocity for HS, (c) Streamwise mean velocity deficit of LS, and (d) Streamwise mean velocity deficit of HS plotted in the center plane $y/D = 0$.

turbulence and mixing in the ABL, the deficits for LS are between 36% and 40%. On the other hand, the mixing for HS is confined to the lower-region of the wake (below the hub height) as the ABL extends slightly above the hub height, resulting in strong asymmetry in the lower and upper-regions (above the hub height) of the wake. The maximum velocity deficit is 30% for HS. Due to mixing the wake expands up to 3D and 2D for LS and HS, respectively. The wake recovery is faster for LS than HS, as expected. Higher the turbulence the faster is the recovery. At $x/D = 7$, LS has recovered with deficits of less than 8%, whereas the deficits of 12% persist for LS at this downstream location.

    In summary, regions of low momentum fluid are created near the blade tips for the WT in ABL under LS. Due to mixing and higher turbulence, high velocity deficits are created both in the lower- and upper-regions of the near-wake region. The wake recovery is fast due to mixing. On the other hand, for the WT in ABL under HS, asymmetric wake develops with higher

deficits in the lower-region of the wake. As mixing is confined to region within the ABL, hence the wake recovery is slower in the upper-region of the wake, which is outside the ABL for HS.

2. Mean shear

Wind shear is the primary source of turbulence in stable stratified ABL. As LS and HS clearly show differences in the mean velocity deficit, now the question arises as to what the differences are in the turbulence generated in the wake region. We next investigate the TKE production, turbulence damping, and the TKE generated in the WT wake. For this purpose, shear stress $(\overline{u'w'})$, mean shear $(\frac{dU}{dz})$, TKE production $(-\overline{u'w'}\frac{dU}{dz})$, mean temperature gradient $(\frac{dT}{dz})$, and TKE are analyzed.

The contours of mean wind shear $(\frac{d\overline{U}}{dz})$ are presented in Fig. 7. The wind shear is almost uniform between the lower- and upper-tips of the blade for LS. Vertical shear reversal occurs just above the LLJ, which is slightly above the WT. For HS, the shear acting on the lower- and upper-tip is quite different. The lower-tip of the blade is subjected to high shear and the upper-tip is outside the ABL. Further, vertical shear reversal occurs within the WT domain as the LLJ occur near the hub height. Thus, the WT under high stratification is subjected to wind with non-uniform vertical shear. The significant differences LS and HS are that the vertical shear acting on the lower-tip is higher for the HS than for the LS in the near-wake region. The vertical shear reversal (i.e., from negative to positive) occurs above the WT for LS and near the hub height for HS. A negative shear contributes to TKE production, and a positive shear damps the TKE production, thus suggesting that as shear is higher for the HS, hence shear-induced damping occurs within the WT wake region.
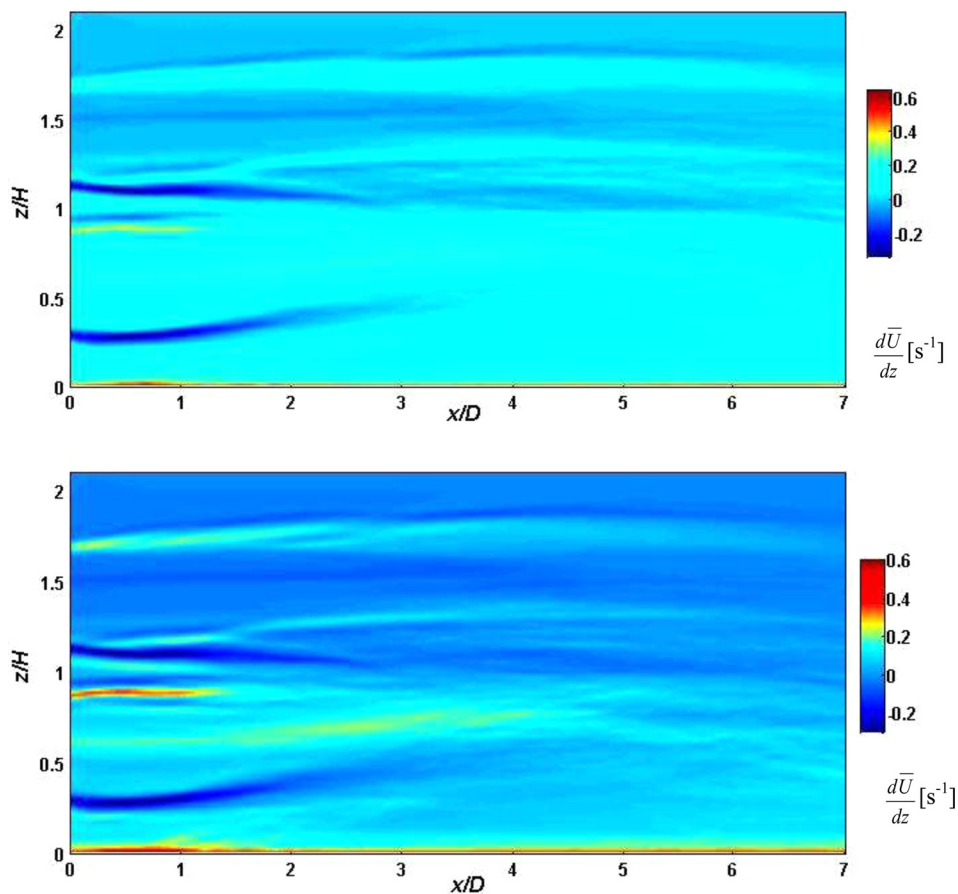

FIG. 7. Mean vertical shear profile: (a) LS and (b) HS plotted at the center plane $y/D = 0$.

3. Reynolds stress, TKE, turbulence production

Reynolds stresses are mechanisms which transfer energy from the mean flow to turbulence. Hence, to understand the transfer of energy process, the contours of shear stress $\overline{(u'w')}$ are presented in Fig. 8. Due to the tip and root vortices, high shear stresses are present near the blade tips of the WT. Difference in $\overline{u'w'}$ between LS and HS arises downstream of the WT. High shear stress due to the root vortices persists up to 7D for LS. As suggested in previous studies by Sotiropoulos *et al.* (2014), the meandering of root vortex leads to a sustained and an enhanced shear stress. Similar to the LS, the root vortex persists up to 7D for HS, but only in the lower-region (below the hub) of the wake. However, the root vortex in the upper-region (above the hub height) is annihilated due to vertical shear reversal at this height. At the lower-tip, high $\overline{u'w'}$ is present between $x/D = 1$–3 for both the cases. Clearly indicating generation of a shear layer is due to the tip vortex. In the lower-region of the wake, $\overline{u'w'}$ increases between $x/D = 3$–6 for both the cases. This is attributed due to shear stress generation from the interaction of the tip and the root vortices. The shear stress at the upper-tip is distinct between LS and HS. The differences arise as turbulence is almost negligible above the hub height. Therefore, high $\overline{u'w'}$ is present only up to the hub height of the WT, with no significant turbulent stresses above the LLJ height.

Fig. 9 shows the TKE shear production $(-\overline{u'w'}\frac{dU}{dz})$ at the center plane, i.e., $y/D = 0$. As seen from the shear stress contours the root and the tip vortices contribute to TKE production. TKE production occurs at the lower- and upper-tips and at the hub height. The TKE generated due to root vortices persists to a way into the wake. Another source of turbulence production is the interaction of the tip and the root vortices in the lower-region of the wake. Further, high TKE production is evident at $x/D = 3$ near the upper-tip for LS. Now, the question arises as to what is the cause of the TKE production at $x/D = 3.0$. We will investigate further in Sec. V B.

Finally, we present the TKE contours in Fig. 10. For LS, close to the WT, distinct peaks are present at the lower- and the upper-tips and at the hub height. Further downstream $(x/D = 4)$, the distinct peaks disappear and a plateau of high TKE appears between the blade tips as seen in Fig. 10(a). Around $x/D = 6$ high TKE is present near the upper-tip. On the other hand, for HS the presence of WT results in concentrated high TKE near the blade-tips and at
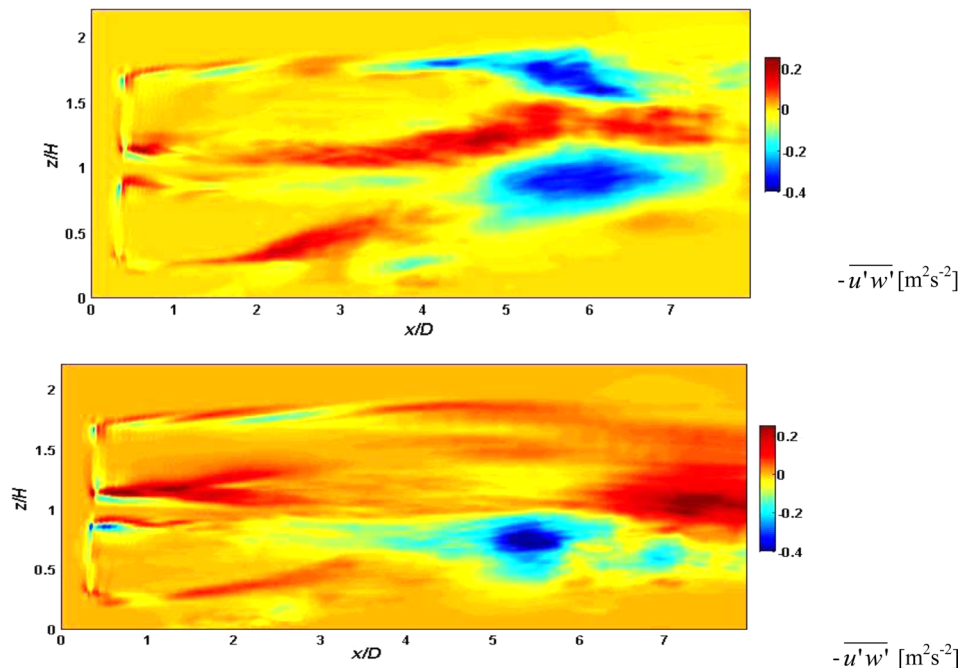

FIG. 8. Contours of shear stress $(-\overline{u'w'})$ for (a) LS and (b) HS at the center plane, $y/D = 0$.
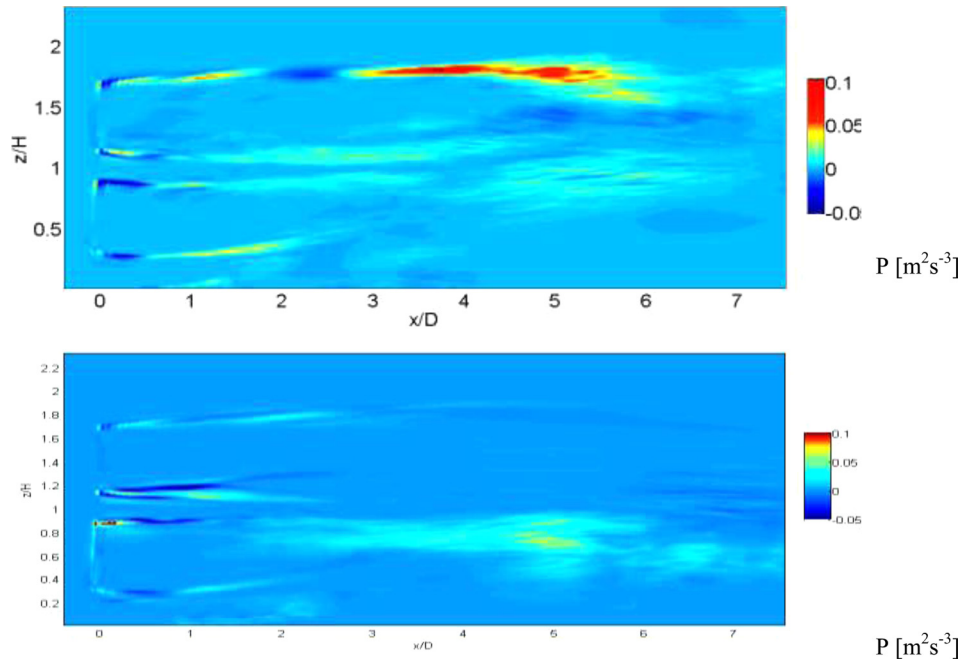
FIG. 9. TKE shear production contours for (a) LS and (b) HS at the center plane, $y/D = 0$.

the hub height. However, further downstream TKE at the upper-tip diminishes very quickly. Distinct TKE peaks start appearing downstream of the WT.

B. Turbulence structures

Analysis of energetics has revealed that near wake turbulence is dominated by TKE production at the location of the LLJ for both LS and HS. As the LLJ occur within the WT
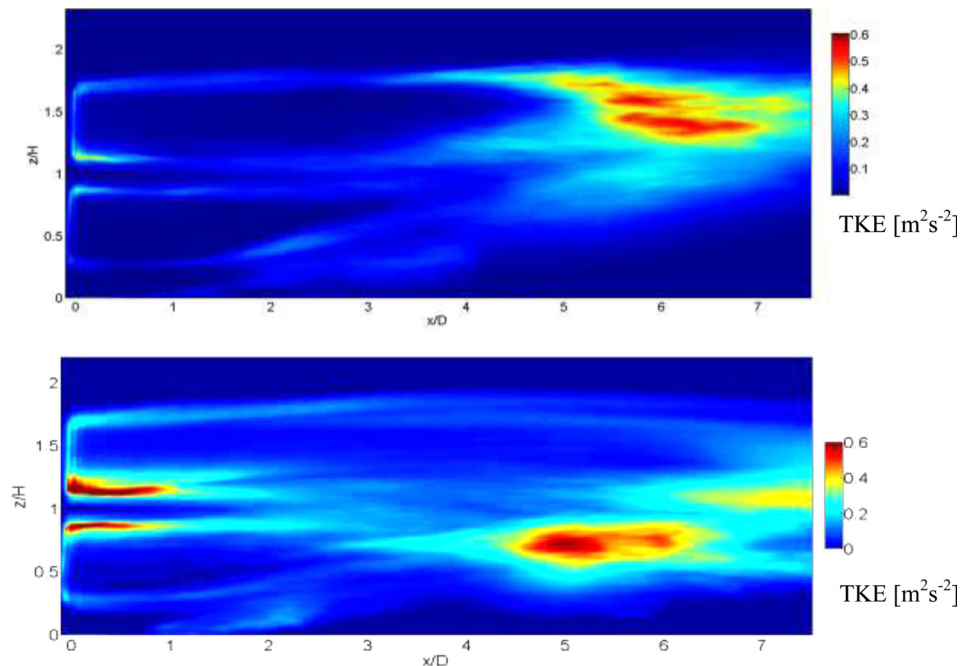

FIG. 10. TKE contours for (a) LS and (b) HS at the center plane, $y/D = 0$.

domain, turbulence mixing is limited and concentrated at the LLJ height for HS. However, for LS, the TKE is distributed throughout the WT height. Next, we focus on the nature of the turbulent structures to complete the picture obtained from the energetics.

1. Velocity structures

Fig. 11 shows the instantaneous velocity in the *y-z* plane at various locations downstream of the WT for HS. High velocities associated with the LLJ are present near the hub height. These velocities in turn result in strong velocity gradients or vertical shear at $x/D = 1$ as seen in Fig. 11(a). Mean shear generates turbulence which results in mixing. In Fig. 11(b) at $x/D = 3$ the LLJ act as barrier resulting strong mixing being confined up to $z = 1.0$. In Fig. 11(c) further downstream from the WT, the flow is well mixed at $x/D = 5$. At $x/D = 6$ from the WT, the wake is still dominant as seen in Fig. 11(d). The wake persists up to 8D (figure not shown) before the flow recovers to the ABL state without any signatures of the WT. It is clear that strong mixing is present only around the hub height, and does not extend to the blade tips. This is consistent with our analysis from the energetics which revealed that TKE production and TKE is concentrated near the hub height, and hence turbulence mixing in the wake region is dominant only at these heights.

Fig. 12 shows the instantaneous velocity in the *y-z* plane for LS. In Fig. 12(a) at $x = 1D$ from the WT, the mean structure of the boundary layer with velocity gradients throughout the WT domain is clearly seen. The LLJ occur at $z/H = 2$ which is above the WT. As strong shear is present throughout the ABL, hence both the upper- and lower-tips of the blade are subjected
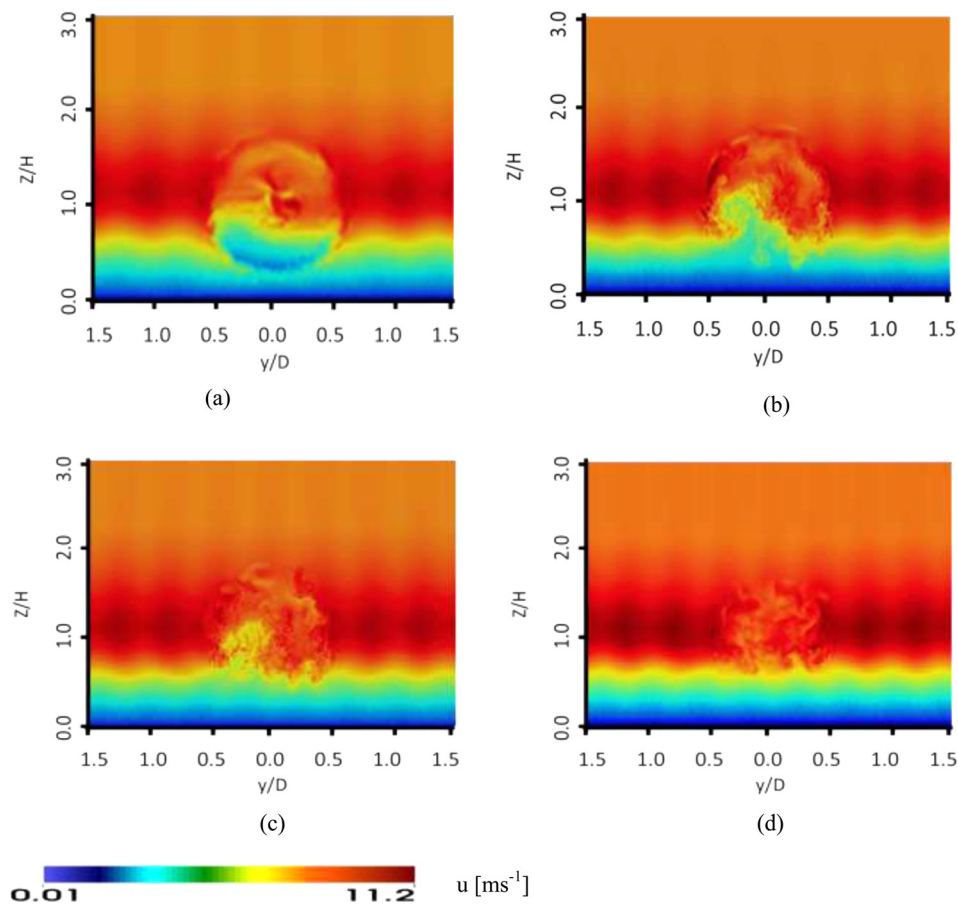

FIG. 11. Instantaneous streamwise velocity in the *y-z* plane at (a) $x/D = 1$, (b) $x/D = 3$, (c) $x/D = 5$, and (d) $x/D = 6$ from the WT for HS.
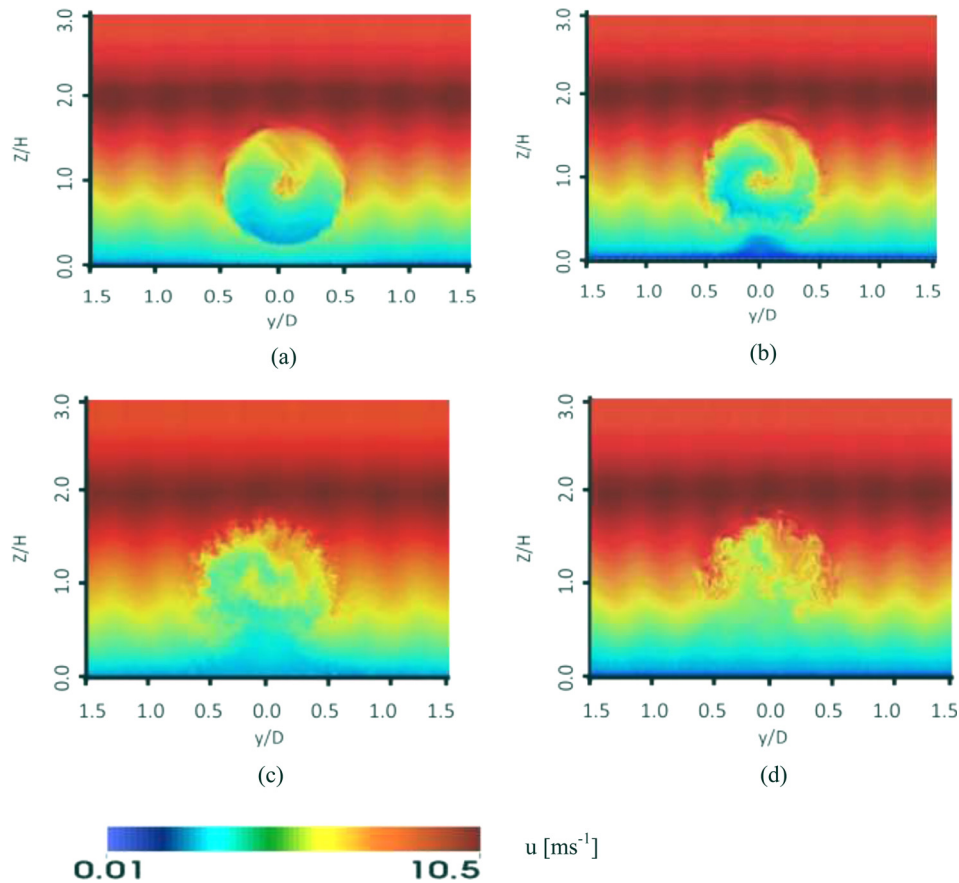
FIG. 12. Instantaneous streamwise velocity in the y-z plane at (a) $x/D = 1$, (b) $x/D = 3$, (c) $x/D = 5$, and (d) $x/D = 6$ from the WT for LS.

to shear. The mean shear generates turbulence resulting in mixing, however, unlike HS, where TKE production and TKE are concentrated near the hub height, the energetics has revealed that TKE is distributed throughout the region between the WT blade tips. At $x/D = 3$ downstream from the WT as seen in Fig. 12(b), the wake region between the lower- and upper-tips is now well mixed. Strong turbulent mixing at $x/D = 3$ is clearly seen with large counter-rotating eddies of size commensurate with WT height. Wake recovery is much faster than HS as seen in Fig. 12(c) at $x/D = 5$. At $x/D = 6$, the signature of the WT is almost negligible as seen in Fig. 12(d). It should be noted that well-defined periodic structure is observed in the y-direction, which arises due to the random perturbations that have been applied to initiate turbulence.

2. Blade tip vortices and root vortex

In Fig. 13, we present the vortex structures that we extracted using the λ_2 vortex detection criterion of Jeong and Hussain (1995). As seen in Fig. 13, the three blades of the WT create three similar tip vortices, one for each blade. The tip vortex follows a helical trajectory, the helical vortex filament is initially smooth, it develops undulations, and it begins to interact with neighboring vortex filaments. This mutual interaction has been observed in similar studies for uniform inlet flow (Sorensen, 2011). Beyond this region, turbulence dominates the previously distinct stable vortex structures. The instability likely results in deforming the tip vortex and where turbulence starts to dominate. The influence of the adjacent helical filaments causes them to roll up around each other, eventually leading to destabilization of the vortex, and also as observed by Sherry et al. (2013) and Kang et al. (2014).

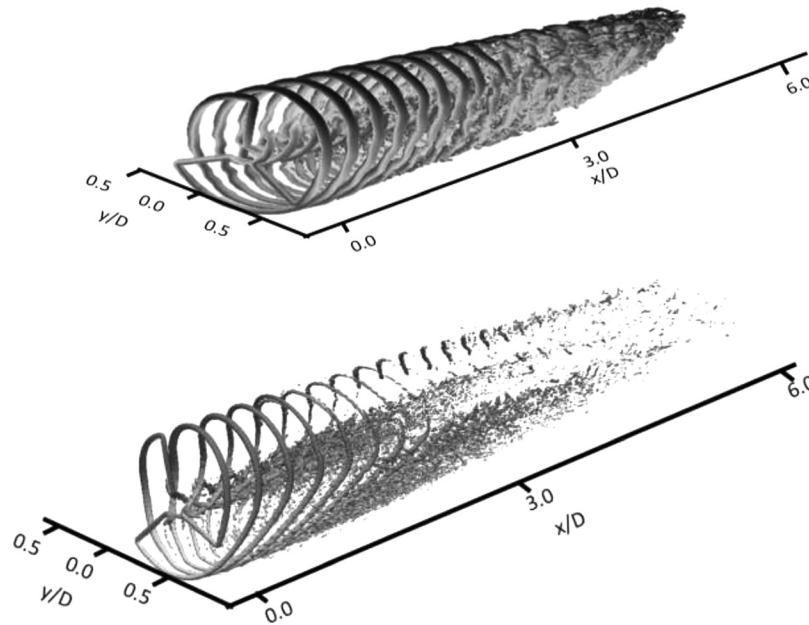FIG. 13. Using the λ_2 vortex detection criterion to extract the tip and hub vortex for (top) LS and (bottom) HS.

For HS (see Fig. 13(b)), the vortex filament experiences large shear at the lower-tip with negligible shear at the upper-tip. Due to height-varying shear acting on the blade tips, the vortex is now stretched to a larger extent resulting in an increased helical pitch. Destabilization of the vortex occurs much earlier than LS. To clearly see the differences in helical pitch due to the difference in ABL characteristics between HS and LS, we plot the vortex filament from a single blade in Fig. 14. The stretching of the helical vortex filament is significantly different for the two cases. Nearly constant vertical shear acts on the WT blades for the LS case, whereas non-uniform vertical shear exists with high shear acting on the lower-tip and negligible shear on the upper-tip for the HS case. Hence, the vortex filament is significantly stretched.

A sliced view of the vorticity field in the x-z plane is shown in Fig. 15. For LS, the merging of vortices is present when the neighboring vortex filaments approach each other. The results are similar to that observed by Sherry *et al*. (2013) in which the neighboring filaments interact with each other and move as a single blob of vorticity at a similar tip speed ratio of 5. Although the merging of vortices through mutual induction has been observed for uniform flow, this is the first time we confirm it for atmospheric mean conditions. The merging occurs around $x/D = 3$. The merged vortices move as a blob and around $x/D = 5.0$ significant instabilities are apparent. Similar trends have also been observed from TKE shear production analysis (Fig. 9(a)). It was seen between $x/D = 3$–5 there is a region of high TKE production. It is clear
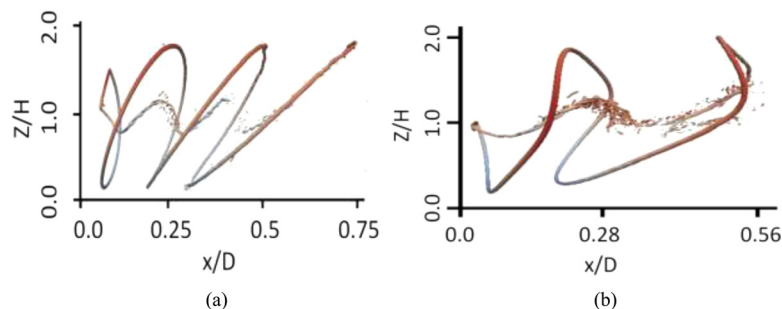

FIG. 14. Tracking the tip-vortex of a single blade WT for (a) LS and (b) HS. Color represents the velocity contours.
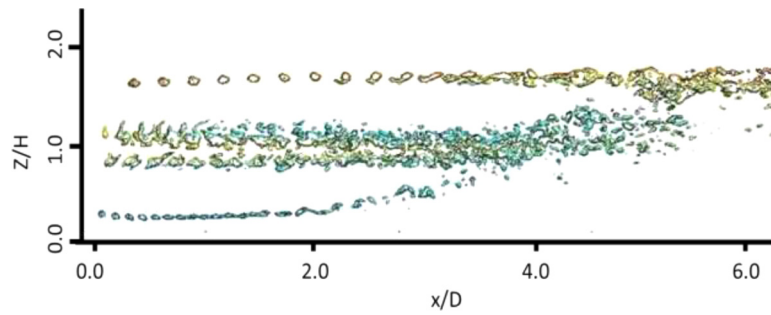
FIG. 15. Vorticity field in *x-z* plane at the WT for LS. The vortex filaments with fixed spacing start coming close together with merging occurring at $x/D = 3$.

that merging of the vortices results in TKE production thus generating TKE. Due to TKE generation, the blob undergoes instability. Vortex merging is a source of flow instability. A similar trend can also be seen from the TKE contours (Fig. 10(a)). A region of high TKE is seen between $x/D = 5$–7, which coincidently corresponds to the region where the merged vortex blob becomes unstable (Fig. 15).

For HS, the merging of the tip vortices is not clearly noticeable. A possible explanation is that as the tip speed ratio is low for HS (3.5 at the hub height) due to high jet velocity at the hub height, and hence the helical pitch of the vortex filaments is higher than that required for the mutual interference between these elements.

3. Vorticity fields

In order to get a better understanding of the strength and the nature of the tip vortices, we next look into the streamwise, wall-normal, and spanwise vorticity fields. We present spanwise vorticity (ω_y) contours in the *x-z* plane in Fig. 16. For LS, wind shear acting on the blade of the WT forms a strong shear layer at the blade tips. The shear layer developed at the lower-tip is strong and it interacts with the root vortex. The strong shear layer that develops at the lower-tip results in shear-layer lift-up in the regions between $x/D = 2$–3. The intense shear layer from the lower-tip interacts with the root vortex resulting in enhancing the shear of the root vortex. The resultant enhanced shear layer now interacts with the shear layer at the upper-tip of the turbine blade around $x/D = 5$. The questions we ask are: Is the shear layer stable or unstable, and
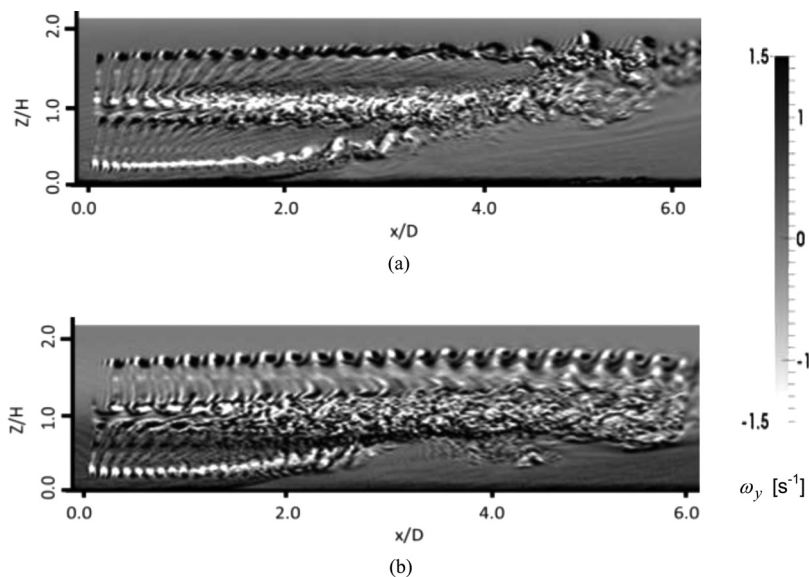

(a)

(b)

FIG. 16. Vorticity contours of spanwise vorticity in the *x-z* plane at y = 0 for (a) LS and (b) HS.
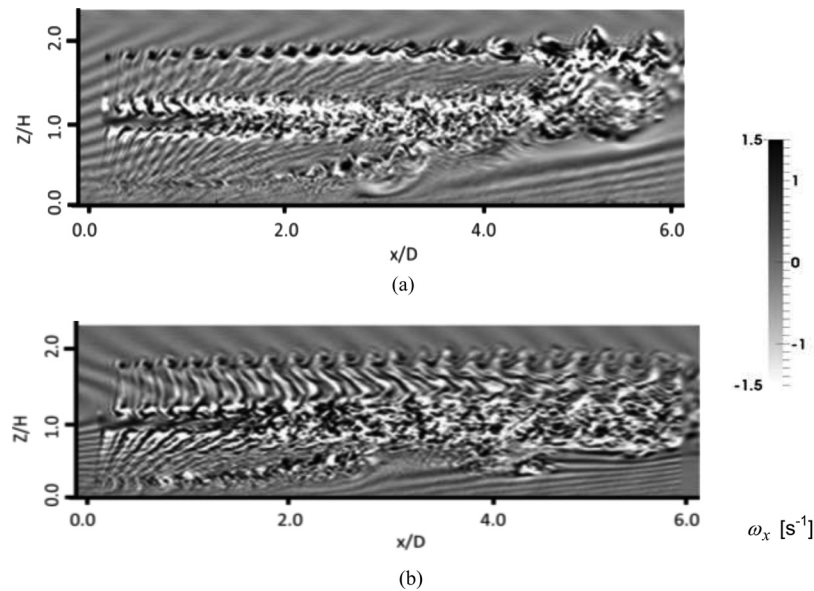
FIG. 17. Vorticity contours of streamwise vorticity in the *x-z* plane at *y* = 0 for (a) LS and (b) HS.

does it generate secondary vorticity? For this purpose, we need to investigate the streamwise vorticity.

For HS, the shear layer formed at the blade tips is significantly different. The shear layer formed near the wall is nearly of the same magnitude as the shear layer formed at the lower-tip, the consequence of which is an interaction between these two shear layers at around $x/D = 1$. The resultant shear layer interacts with the root vortex and merges with it at $x/D = 3$. Differences exist in the shear layer developed at the hub between LS and HS. The helical vortex filament for HS experiences non-uniform shear, thus distorting the vortex filament quite significantly. The high shear at the lower-tip for HS results in breaking down the shear layer much earlier than LS. At the hub height, vertical shear reversal prevents the interaction of the root vortex with the shear layer formed at the upper-tip of the turbine blade.

We present streamwise vorticity fields (ω_x) in the *x-z* plane at $y = 0$ in Fig. 17. Around the same location, the shear layer lift-up has started, i.e., $x/D = 2$–3, and a dominant streamwise vortex is present. It clearly demonstrates the presence of secondary instability due to an unstable shear layer. The consequence of the unstable shear layer is mutual interaction of the neighboring vortex filaments resulting in merging of the vortices. The interaction of the shear layer from the lower-tip vortex with the root vortex also results in regions of secondary vorticity extending from the hub height to the upper-tip of the WT. Right after the merging of the vortices, a strong streamwise vortex is present around $x/D = 5$ near the upper-tip.

For the HS case, ω_x is organized at the upper-tip, whereas it is more irregular near the lower-tip. The intensity of ω_x is high near the hub region, whereas it is less intense near the blade-tip regions. This indicates that the secondary instability associated with the root vortex is dominant in this case. It is interesting to note that TKE increases between $x/D = 4$–6 (Fig. 10(b)), thus indicating the instability of the root vortex.

VI. CONCLUSION

Full-scale horizontal axis wind turbines operate in the atmospheric boundary layer, and an accurate representation of ABL initial conditions is important for realistic prediction of wake effects behind the turbine. A study has been conducted to explore the role of mean forcings of the atmosphere—mean velocity, temperature, the surface momentum, temperature-flux—on the turbulence developed in the wake of WT. Actuator line model based LES tool has been used to simulate WT in stable atmospheric boundary layer subjected to low and high atmospheric

stratifications. Precursor ABL simulations have been performed to obtain the mean forcings of the atmosphere, which are then introduced as initial conditions for the WT simulations.

LLJ influence the turbulence energetics as well as the large-scale vortex structures in the wake. Turbulence generated in the wake region behind the WT is a balance of turbulence production due to shear and damping due to buoyancy. Changes in atmospheric stability alter the location and strength of LLJ resulting in modified $\frac{dU}{dz}$ and $\frac{dT}{dz}$ profiles, and therefore they influence both the shear production as well as buoyancy induced damping. The differences between characteristics of ABL under LS and HS that are relevant for turbulence generated behind WT are quite significant. The low-stratified ABL is characterized by LLJ that occur above the WT height resulting in uniform wind shear acting on both the upper- and lower-blade tips. The scales of turbulence mixing commensurate with WT height resulting in a mixed layer behind the WT. High TKE results in increased mixing, and thus a faster wake recovery to the original ABL state. In the high-stratified ABL, LLJ occur at the hub-height resulting in an asymmetric wake with strong deficits in the lower wake region. The mixing is confined to region below the hub-height resulting in weaker mixing than LS. Thus, it results in slowing down the wake recovery.

The tip vortex undergoes mutual induction mode of instability resulting in merging of vortices. Vortex merging generates TKE and shear stress leading to instability of the tip vortex. A strong and unstable shear layer develops near the lower-tip which interacts with the root vortex generating secondary instability. The root vortex undergoes instability due to the interaction of the tip and root vortex, and generating high shear stress and TKE.

The present study did not include atmospheric processes such as the transfer of solar and terrestrial radiation between the surface and the atmosphere, formation and evolution of cloud, microphysical properties, and surface interactions, including the exchange of radiation as well as sensible and latent heats. We added artificial turbulence at the inlet of the domain which is homogenous, stationary, Gaussian and spatially periodic in nature. This is one of the limitations of the present study as only realistic large-scale forcings of the atmosphere have been included in the study. In our future study, we will include the effects of atmospheric turbulence on the wake effects of WT.

It should be noted that turbine loadings, and also fatigue and failure rates are altered due to the differences in the wind conditions under different stratifications. Characterizing the wake based on tip-speed ratio is not sufficient for WT operating under ABL conditions; hence, in addition to the turbine loadings, the wind shear and temperature gradient are additional metrics that dictate the wake turbulence.

In conclusion, the large-scale forcings of thermally stratified atmospheric boundary characterized by shear- and buoyancy-driven turbulence significantly influence the wake structure of a wind turbine. The study is quite significant as it clearly demonstrates the implications of the underlying atmospheric state on the WT wake. Further, the study indicates a need for a paradigm shift from WT studies based on idealistic conditions to those using realistic ABL forcings.

ACKNOWLEDGMENTS

Banta, R., "Stable-boundary layer regimes from the perspective of the low-level jet," Acta Geophys. **56**(1), 58–87 (2008).

Basu, S. and Porte-Agel, F., "Large-eddy simulation of stably stratified atmospheric boundary layer turbulence: A scale-dependent dynamic modeling approach," J. Atmos. Sci. **63**, 2074–2090 (2005).

Basu, S., Holtslag, A., Wiel, V., Moene, A., and Steveneveld, G., "An inconvenient truth about using sensible heat flux as a surface boundary condition in models under stably stratified regimes," Acta Geophys. **56**(1), 88–99 (2008).

Beare, R. J., Macvean, M. K., Holtslag, A. A. M., Cuxart, J., Esau, I., Golaz, J. C., Jimenez, M. A., Khairoutdinov, M., Kosovic, B., Lewellen, D., Lund, T. S., Lundquist, J., Mccabe, A., Moene, A., Noh, Y., Raasch, S., and Sullivan, P., "An intercomparison of large-eddy simulations of the stable boundary layer," Boundary-Layer Meteorol. **118**, 247–272 (2006).

Chamorro, L. P. and Port E-Agel, F., "A wind-tunnel investigation of wind-turbine wakes: boundary-layer turbulence effects," Boundary-Layer Meteorol. **132**(1), 129–149 (2009).

Churchfield, M., Lee, S., and Moriarty, P., "Adding complex terrain adding complex terrain and stable atmospheric condition capability to the OpenFOAM- based flow solver of the simulator for on/offshore wind farm applications (SOWFA)," paper presented at the 1st Symposium on OpenFoam in Wind Energy Oldenburg, Germany, March 20–21 (2013).

Churchfield, M. J., Li, Y., and Moriarty, P. J., "A large eddy simulation study of wake propagation and power production in an array of tidal-current turbines," in 9th European Wave and Tidal Energy Conference, September 4–9, Southampton, England (2011), Paper No. NREL/CP-5000-51765.

Cuxart, J., Bougeault, P., and Redelsperger, J. L., "A turbulence scheme allowing for mesoscale and large-eddy simulations," Q. J. R. Meteorol. Soc. **126**, 1–30 (2000).

Esau, I., "Simulation of Ekman boundary layers by large Eddy model with dynamic mixed subfilter closure," J. Environ. Fluid Mech. **4**(3), 273–303 (2004).

Felli, M., Camussi, R., and Di Felice, F., "Mechanisms of evolution of the propeller wake in the transition and far fields," J. Fluid Mech. **682**, 5–53 (2011).

Hu, H., Yang, Z., and Sarkar, P., "Dynamic wind loads and wake characteristics of a wind turbine model in an atmospheric boundary layer wind," Exp. Fluids **52**, 1277–1294 (2012).

Huang, J. and Bou-Zeid, E., "Turbulence and vertical fluxes in the stable atmospheric boundary layer Part I: A large-eddy simulation study," J. Atmos. Sci. **70**(6), 1513–1527 (2013).

Ivanell, S., Mikkelsen, R., Sorensen, J. N., and Henningson, D., "Stability analysis of the tip vortices of a wind turbine," Wind Energy **13**, 705–715 (2010).

Jeong, J. and Hussain, F., "On the identification of a vortex," J. Fluid Mech. **285**, 69–94 (1995).

Jha, P., Churchfield, M. J., Moriarty, P. J., and Schmitz, S., "Guidelines for actuator line modeling of wind turbines on large-Eddy simulation-type grids," ASME J. Solar Energy Eng. **136**, 031003 (2014).

Kang, S., Yang, X., and Sotiropoulos, F., "On the onset of wake meandering for an axial flow turbine in a turbulent open channel flow," J. Fluid Mech. **744**, 376–403 (2014).

Khairoutdinov, M. F. and Randall, D. A., "Cloud resolving modeling of the ARM summer 1997: Model formulation, results, uncertainties, and sensitivities," J. Atmos. Sci. **60**, 607–625 (2003).

Kosovic, B. and Curry, J. A., "A large-Eddy simulation study of a quasi-steady stably-stratified atmospheric boundary layer," J. Atmos. Sci. **57**, 1052–1068 (2000).

Lewellen, D. C. and Lewellen, W. S., "Large-Eddy boundary layer entrainment," J. Atmos. Sci. **55**, 2645–2665 (1998).

Lilly, D. K., "The representation of small-scale turbulence in numerical simulation experiments," in *Proceedings of IBM Scientific Computing Symposium on Environmental Sciences*, White Plains, NY, IBM Data Process. Div. (1967).

Lu, H. and Porte-Agel, F., "Large-Eddy simulation of a very large wind farm in a stable atmospheric boundary layer," Phys. Fluids **23**, 065101 (2011).

Massouh, F. and Dobrev, I., "Exploration of the vortex wake behind of wind turbine rotor," J. Phys.: Conf. Ser. **75**, 012036 (2007).

Mirocha, J., Kosovic, B., Aitken, M., and Lundquist, J., "Implementation of a generalized actuator disk wind turbine model into the weather research and forecasting model for large-eddy simulation applications," J. Renewable Sustainable Energy **6**, 013104 (2014).

Nieuwstadt, F. T. M., "The turbulent structure of the stable, nocturnal boundary layer," J. Atmos. Sci. **41**(14), 2202–2216 (1984).

Ohya, Y., Neff, D., and Meroney, R., "Turbulence structure in a stratified boundary layer under stable conditions," Boundary-Layer Meteorol. **83**, 139–161 (1997).

Okulov, V. L. and Sørensen, J. N., "Stability of helical tip vortices in a rotor far wake," J. Fluid Mech. **576**, 1–25 (2007).

Poulos, G. S., Blumen, W., Fritts, D. C., Lundquist, J. K., Sun, J., Burns, S. P., and Jensen, M., "CASES-99: A comprehensive investigation of the stable nocturnal boundary layer," Bull. Am. Meteorol. Soc. **83**(4), 555 (2002).

Raasch, S. and Etling, D., "Numerical simulations of rotating turbulent thermal convection," Phys. Atmos. **64**, 185–199 (1991).

Sherry, M., Nemes, A., Jacono, D. L., Blackburn, H., and Sheridan, J., "The interaction of helical tip and root vortices in a wind turbine wake," Phys. Fluids **25**(11), 117102 (2013).

Sorensen, J. N., "Instability of helical tip vortices in rotor wakes," J. Fluid Mech. **682**, 1–4 (2011).

Sørensen, J. N. and Shen, W. Z., "Numerical modeling of wind turbine wakes," J. Fluids Eng. **124**, 393–399 (2002).

Stoll, R. and Porte-Agel, F., "Large-eddy simulation of the stable atmospheric boundary layer using dynamic models with different averaging schemes," Boundary-Layer Meteorol. **126**, 1–28 (2008).

Sullivan, P. P., McWilliams, J. C., and Moeng, C.-H., "A subgrid-scale model for large-Eddy simulation of planetary boundary-layer flows," Boundary-Layer Meteorol. **71**, 247–276 (1994).

Troldborg, N., Larsen, G. C., Madsen, H. A., Hansen, K. S., Sørensen, J. N., and Mikkelsen, R., "Numerical simulations of wake interactions between two wind turbines at various inflow conditions," Wind Energy **13**, 86 (2010).

Troldborg, N., Sørensen, J. N., and Mikkelsen, R., "Actuator line simulation of wake of wind turbine operating in turbulent inflow," J. Phys.: Conf. Ser. **75**, 012063 (2007).

Vermeer, L. J., Sorensen, J. N., and Crespo, A., "Wind turbine wake aerodynamics," Prog. Aerosp. Sci. **39**, 467–510 (2003).

Whale, J., Papadopoulos, K. H., Anderson, C. G., and Skyner, D. J., "A study of the near wake structure of a wind turbine comparing measurements from laboratory and full-scale experiments," Solar Energy **56**(6), 621–633 (1996).

Wharton, S. and Lundquist, J., "Atmospheric stability effects wind turbine power collection," Environ. Res. Lett. **7**, 014005 (2012).

Widnall, S. E., "The stability of a helical vortex filament," J. Fluid Mech. **54**(4), 641–663 (1972).

Yang, Z., Sarkar, P., and Hu, H., "Visualization of the tip vortices in a wind turbine wake," J. Visualization **15**(1), 39–44 (2012).

Zahle, F. and Sørensen, J., "On the influence of far-wake resolution on wind turbine flow simulations," J. Phys.: Conf. Ser. **75**, 012042 (2007).

Zhang, W., Markfort, C. D., and Porte E-Agel, F., "Near-wake flow structure downwind of a wind turbine in a turbulent boundary layer," Exp. Fluids **52**(5), 1219–1235 (2012).

Zhou, B. and Chow, F., "Turbulence modeling for the stable atmospheric boundary layer and implications for wind energy," Flow Turbul. Combust. **88**, 255–277 (2012).